Iron and Manganese Co-doped Mesoporous Carbon-based Catalysts via Template-Assisted Synthesis for Proton Exchange Membrane Fuel Cells

Kaarel Kisand, Ave Sarapuu, Srinu Akula, Arvo Kikas, Alexey Treshchalov, Maike Käärik, Helle-Mai Piirsoo, Jekaterina Kozlova, Jaan Aruväli, Jaan Leis, et al.

Iron and Manganese Co-doped Mesoporous Carbon-based Catalysts via Template-Assisted Synthesis for Proton Exchange Membrane Fuel Cells

Kaarel Kisand[a], Ave Sarapuu[a], Srinu Akula[a], Arvo Kikas[b], Alexey Treshchalov[b], Maike Käärik[a], Helle-Mai Piirsoo[b], Jekaterina Kozlova[b], Jaan Aruväli[c], Jaan Leis[a], Vambola Kisand[b], Kaupo Kukli[b], Ghenwa El Chawich[d], Frédéric Jaouen[d], Sara Cavaliere[d], Kaido Tammeveski[a*]

[a]*Institute of Chemistry, University of Tartu, Ravila 14a, 50411 Tartu, Estonia*

[b]*Institute of Physics, University of Tartu, W. Ostwald Str. 1, 50411 Tartu, Estonia*

[c]*Institute of Ecology and Earth Sciences, University of Tartu, Vanemuise 46, 51014 Tartu, Estonia*

[d]*ICGM, Univ. Montpellier, CNRS, ENSCM, Montpellier, France*

Abstract

This work explores a novel and sustainable synthesis strategy for developing platinum-group metal (PGM)-free catalysts with high electrocatalytic activity, emphasizing the significance of hierarchically porous structures to improve electrocatalytic performance. We present an easily scalable method that utilizes magnesium salt as the precursor of sacrificial template to synthesize mesoporous carbon-based catalysts. The catalysts are doped with nitrogen and iron, while manganese is added to increase the stability of the catalyst under highly corrosive acidic conditions. The electrochemical oxygen reduction reaction (ORR) is investigated in acidic media using the rotating disk electrode technique. The electrocatalytic activity of the prepared catalysts is evaluated in proton exchange membrane fuel cell (PEMFC), where a significant increase in performance is achieved with the hierarchically porous carbon catalyst. The results demonstrate the potential of these catalysts as efficient and durable alternatives to PGM-based cathode catalysts in PEMFCs.

***Keywords*:** oxygen reduction reaction, M-N-C catalysts, PGM-free catalysts, sacrificial template, mesoporous carbon, proton-exchange membrane fuel cell

[*]Corresponding author. Tel.: +372 7375168; E-mail: kaido.tammeveski@ut.ee (K. Tammeveski)

1. Introduction

The operational efficiency of proton exchange membrane fuel cells (PEMFCs) poses challenges for their broader adoption, stemming from constraints related to the cathode and the oxygen reduction reaction (ORR) in low-pH environment, where the sluggish kinetics heavily depend on platinum-group metal (PGM) catalysts. Reducing the PGM loading is a viable option to reduce costs, however it tends to decrease the durability of the catalyst. As a result, simultaneously attaining the durability goal set by the U.S. Department of Energy (DOE) while meeting cost and PGM loading objectives, is a major challenge [1]. In addition, even while using reduced loadings, such as 0.125 mg_{Pt} cm^{-2}, PGM-based catalysts continue to account for slightly under half of the entire cost of a PEMFC stack intended for automotive application [2]. Due to this, a lot of research has been invested into finding alternative PGM-free electrocatalysts for ORR.

In the past years, the advances in synthesis methodologies have resulted in the development of transition metal-nitrogen-carbon (M-N-C) catalysts for ORR electrocatalysis, mostly composed of M-N_x sites, where M is a 3d transition metal, with minimal amount of metal nanoparticles [3–7]. Conversely, it is also possible to create a different type of pyrolyzed PGM-free catalysts with high metal contents. These catalysts consist of metallic (or metal carbide) species surrounded by a protective carbon layer known as metal@N-C sites [8–11]. These sites typically exhibit a lower turnover frequency (TOF) for ORR compared to M-N_x sites, especially in acidic medium. However, they can achieve a higher loading of metal, compensating for the lower TOF [12]. Apart from Fe-doped catalysts, there have been investigations on Mn-doped catalysts in promoting the ORR kinetics, while preventing Fenton reactions [13–15]. Li et al. showed that Mn-containing catalysts display enhanced stability under a harsh oxidative environment [15]. Such catalysts frequently demonstrate lower kinetic performance when compared with similarly prepared iron-containing catalysts. To address the shortcomings associated with single-site catalysts, particularly in terms of their insufficient activity and stability, an alternative strategy involves the development of catalysts that embed dual or multiple metal sites [16–19].

Although PGM-free electrocatalysts offer benefits such as low cost and improved resistance to contaminants [20], they present a challenge due to their lower volumetric activity. Numerous investigations have highlighted the pivotal role of hierarchically porous structures of carbon-based catalyst materials in enhancing electrocatalytic performance [21–24]. This becomes particularly pronounced in the case of membrane electrode assemblies (MEAs), due

to the intricate electrode configurations. As such, it is crucial to understand the distinct functions played by micro-, meso-, and macropores within the catalyst material. An illustration of this is the research conducted by Atanassov and co-workers, who successfully developed a series of Fe-N-C catalysts with a structured micro-mesoporous arrangement using the silica-templating technique [25,26]. However, the removal of the silica template typically requires the use of hydrofluoric acid or other fluorinated compounds, which is the primary concern and disadvantage associated with this method. A viable alternative to silica-based templates is to employ a templating approach, in which inorganic nanoparticles (like MgO or $CaCO_3$) or their precursor salts and organic polymer precursor or coordination polymer are heat-treated, resulting in a carbon framework containing embedded metal oxide nanoparticles [27–30]. Inagaki et al. [31] were the first to use a simple procedure where a carbon precursor and thermally unstable magnesium compounds like acetate or citrate were pyrolyzed together, leading to the decomposition of precursor salt and formation of the template nanoparticles. Removing these inorganic components through a simple washing process with dilute hydrochloric acid yielded a hierarchically porous nanocarbon material with a high specific surface area and mesoporosity.

In the present study, we introduce a straightforward and scalable Mg-template based approach for preparing mesoporous carbon electrocatalysts co-doped with nitrogen and iron/manganese. Here, HoneyolTM (a mixture of alkyl resorcinols) acts as the carbon source, dicyandiamide (DCDA), Fe, and Mn salts provide the nitrogen and transition metals, respectively, and magnesium acetate serves as the sacrificial-template precursor. The ORR electrocatalytic activity of the synthesized electrocatalysts was evaluated in a 0.5 M H_2SO_4 electrolyte solution using the rotating disk electrode (RDE) and rotating ring-disk electrode (RRDE) techniques, and their performance as cathode catalysts in PEMFC was evaluated by MEA tests.

2. Experimental

2.1 Preparation of electrocatalysts

The electrocatalysts were prepared by using a previously developed synthesis approach [21]. In brief, Honeyol^{TM} (VKG Oil AS, Estonia) was used as the carbon precursor, DCDA (Sigma-Aldrich) and $Mg(CH_3COO)_2{\cdot}4H_2O$ (98%, Alfa Aesar) were used as the nitrogen and template precursors. The precursors were dissolved in a mixture of Milli-Q water and 2-propanol (at a volume proportion of 1 to 4). Subsequently, iron nitrate or a combination of

iron nitrate and manganese acetate were added to achieve a metal-to-Honeyol mass ratio of 1:20 (as shown in Table 1). The mixture was oven dried at 60 °C, after which the mixture was ground using a pestle and mortar. The homogenized precursor mix was pyrolyzed at 800 °C for 2 h in a nitrogen atmosphere with a ramping rate of 10 °C min^{-1}. The products were soaked in 1 M hydrochloric acid (Sigma-Aldrich) for 2 h at room temperature to dissolve the Mg-containing template particles and metal-containing nanoparticles. The resulting catalyst materials were thoroughly rinsed with Milli-Q water, dried, and then underwent a second pyrolysis at 800 °C for 1 h in a nitrogen atmosphere with a ramping rate of 50 °C min^{-1}. The resulting catalyst materials were named FeNC-T and FeMnNC-T (catalysts obtained with the addition of Mg-template). For the synthesis of the untemplated material FeNC, a similar synthesis method was used without the inclusion of $Mg(CH_3COO)_2{\cdot}4H_2O$.

Table 1. Amounts of the precursors used in the synthesis of the catalyst materials.

Catalyst	Honeyol (g)	DCDA (g)	$Fe(NO_3)_3{\cdot}9H_2O$ (mg)	$Mn(CH_3COO)_2{\cdot}4H_2O$ (mg)	$Mg(CH_3COO)_2{\cdot}4H_2O$ (g)
FeNC	0.2	2	72.4	-	-
FeNC-T	0.2	2	72.4	-	0.2
FeMnNC-T	0.2	2	50.7	13.4	0.2

2.2 Physicochemical characterization

The electrocatalysts were investigated by various characterization methods described in detail in the Supplementary Material.

2.3 Electrochemical measurements

A glassy carbon (GC) electrode (GC20-SS, Tokai Carbon, Japan) with a geometric surface area of 0.196 cm^2 was used as the working electrode. Before use, the electrode was polished with alumina slurries with particle size of 0.3 μm and 1 μm (Buehler). The catalyst powders (4 mg) were ultrasonically dispersed in a 1 mL mixture of 2-propanol and water (1:1 v/v) along with 20 μl Nafion® solution (5 wt.% in lower alcohols, Aldrich) to prepare the dispersed electrocatalyst ink. It was then drop-coated on a glassy carbon working electrode to achieve a catalyst mass loading of 0.8 mg cm^{-2}. For comparison with a benchmark, the same procedure was followed to coat the GC electrodes with a Pt/C catalyst (20 wt.%, E-TEK), with a total catalyst loading on the electrode of 0.2 mg cm^{-2}.

The electrocatalytic ORR activity of the catalysts was investigated by steady-state measurement in O_2-saturated (99.999%, Linde) 0.5 M H_2SO_4 solution using the rotating disk

electrode method. Electrochemical measurements were conducted in a 3-electrode glass cell with an Autolab potentiostat/galvanostat PGSTAT30 (Metrohm-Autolab, The Netherlands). Potentials were measured relative to a saturated calomel electrode (SCE) and a carbon rod served as the counter electrode. Potentials vs SCE were converted with respect to the reversible hydrogen electrode (RHE): $E_{RHE} = E_{SCE} + 0.258$ V. The electrode rotation rate (ω) ranged from 360 to 1900 rpm, controlled by a CTV101 speed control unit connected to an EDI101 rotator (Radiometer). The background current was recorded in Ar-saturated (99.999%, Linde) 0.5 M H_2SO_4 solution, and these values were subtracted from the experimental oxygen reduction currents. The RDE data were analyzed using the Koutecky-Levich (K-L) equation (1) [32]:

$$\frac{1}{j} = \frac{1}{j_k} + \frac{1}{j_d} = \frac{1}{j_k} - \frac{1}{0.62\mathrm{nF}D_{O_2}^{2/3}\nu^{-1/6}C_{O_2}\omega^{1/2}} \qquad (1)$$

where j is the measured current density, j_k and j_d are the kinetic and diffusion-limited current densities, respectively, F is the Faraday constant (96 485 C mol^{-1}), ω is the rotation rate (rad s^{-1}), D_{O2} is the diffusion coefficient of O_2 (1.8×10^{-5} cm^2 s^{-1}) [33], C_{O2} is the O_2 solubility (1.13×10^{-6} mol cm^{-3}) [33], and ν is the kinematic viscosity of the solution (0.01 cm^2 s^{-1}).

A MSRX speed controller and an AFMSRX rotator (Pine Research, USA) were used for the rotating ring-disc electrode (RRDE) measurement. The electrode setup consisted of a GC disc (with a geometric area of 0.164 cm^2) and platinum ring electrode (Pine Research, USA). The electrodes and ink were prepared identically to the RDE experiments. Similarly to the RDE measurements, the used catalyst mass loading was 0.8 mg cm^{-2}. The ring electrode was held at a constant potential of 1.25 V vs RHE. Before conducting the ORR experiment, three CVs in the potential range of 0.06-1.66 V vs RHE were performed. The collection efficiency (N) of the ring electrode with a value of 0.25, was determined using hexacyanoferrate(III) reduction reaction. The peroxide percentage yield (%H_2O_2) and electron transfer number (n) were calculated by Eqs. (2) and (3):

$$\%\mathrm{H_2O_2} = \frac{\frac{2I_r}{N}}{I_d + \frac{I_r}{N}} \times 100\% \qquad (2)$$

$$n = \frac{4I_d}{I_d + \frac{I_r}{N}} \qquad (3)$$

where I_d is the disk current, I_r is the ring current and N is the collection efficiency of the Pt ring.

For durability testing, according to the guidelines from the U.S. Department of Energy, it is recommended to cycle the cathode potential within a range of 0.60 to 0.95 V vs RHE in an

inert gas atmosphere [34]. However, this methodology results in a relatively minor voltage loss as evidenced by multiple studies [8,35,36], since a significant part of the performance loss is caused by peroxide production or other reactive oxygen species formed during the ORR process [12]. For example, in the experiments conducted by Wu et al. [37], potential cycling in O_2-saturated electrolyte solution resulted in a substantial change of 80 mV in the half-wave potential ($E_{1/2}$) value after only 5000 cycles, while the performance loss in N_2-saturated solution was only 10 mV. Keeping that in mind, in this work the accelerated durability testing was conducted by potential cycling from 0.95 to 0.6 V vs RHE in O_2-saturated 0.5 M H_2SO_4 electrolyte solution at a potential scan rate (ν) of 100 mV s^{-1}. The RDE polarization curves were measured after 1000, 5000, and 10000 potential cycles.

2.4 Membrane electrode assembly construction and fuel cell measurements

For the preparation of the cathode ink, 40 mg of a catalyst (FeNC, FeNC-T, or FeMnNC-T) was dispersed in a mixture of Milli-Q water (1 mL), 2-propanol (2 mL) and 0.52 mL of Nafion® ionomer solution (5 wt.%, Sigma-Aldrich) by sonication in an ice bath for 2 h. A commercial Pt/C catalyst (46.1 wt.% Pt, Tanaka Kikinzoku Kogyo K.K., Japan) was used to prepare the anode electrode with an ionomer-to-catalyst (I/C) ratio of 1:1.

To prepare the MEAs the anode catalyst ink was spray-coated with an airbrush (Paasche®, USA) on a gas diffusion layer (GDL; BB-39, Sigracet) with a loading of 0.25 mg_{Pt} cm^{-2} and dried at 80 °C. Then, the anode GDE was hot-pressed (Carver, USA) with Nafion® NRE-211 membrane at 130 °C for 3 min at 0.3 metric-ton load. After cooling to room temperature, the cathode catalyst layer was spray-coated on the other side of the Nafion membrane until obtaining a cathode catalyst loading of 4.0 mg cm^{-2}. The prepared MEA was assembled along with a Sigracet BB-39 GDL in single cell (Fuel Cell Technologies Inc., USA). The commercial Pt-based cathode was prepared by spray-coating gas diffusion layer (GDL; BB-22, Sigracet) to obtain a loading of 0.25 mg_{Pt} cm^{-2}. The cathode along with the anode and membrane were then hot-pressed to obtain the MEA.

The fuel cell polarization curves were recorded using Greenlight Fuel Cell Test Station (G40 Fuel Cell System, Hydrogenics, Canada) at 80 °C and 2.0 bar backpressures on both the anode and cathode side. The flow rate of H_2 and O_2 gases (fully humidified) was 0.3 NLPM in the PEMFC tests.

3. Results and discussion

3.1 Structural characterization

All the prepared electrocatalysts show a rough and heterogenous structure (Figure S1). However, at higher magnification (Figure S1 a, c and e), it can be noticed that FeNC is smoother and has more sheet-like structures, whereas FeNC-T and FeMnNC-T exhibit a rougher texture. Using scanning transmission electron microscopy (STEM) and EDX mapping in STEM, the morphology and element distribution of the catalyst materials was studied in more detail (Figure 1, S2 and S3). Nanoparticles are visible in the high-angle annular dark field (HAADF) images (Figure S2a-c) with sizes varying from a few nanometers to about 25 nm. Some of these nanoparticles are enclosed in graphitic carbon shells (Figure S2d). According to STEM-EDX mapping (Figure 1a and b), these nanoparticles show intense iron signal. Figure S3 compares the untemplated FeNC and FeNC-T (with added Mg acetate). In the case of FeNC, we observe fewer but at the same time larger metallic nanoparticles, while for FeNC-T the nanoparticles are smaller in size and more evenly distributed throughout the carbon structure, suggesting that Mg acetate affects the dispersion of the metal species. Since the FeMnNC-T catalyst seems to contain even less large iron particles compared to FeNC-T, it appears that the addition of manganese helps to further prevent agglomeration. STEM analysis suggests the presence of finely dispersed metal sites in the carbon structure in the carbon structure, possibly as atomically dispersed M-N_x centers (Figure 1b and f), especially for FeMnNC-T as no agglomerated iron particles can be observed (Figure 1f). For FeNC-T material, in addition to Fe-N_x sites, some agglomerated iron particles can also be observed (Figure 1b). Even after the acid washing process, there is still some uniformly distributed magnesium (Mg) in the material, despite the absence of any large magnesium particles (Figure 1c and g). It has been shown that Mg can also form M-N_x sites, which are resistant to removal by performing acid washing [5].

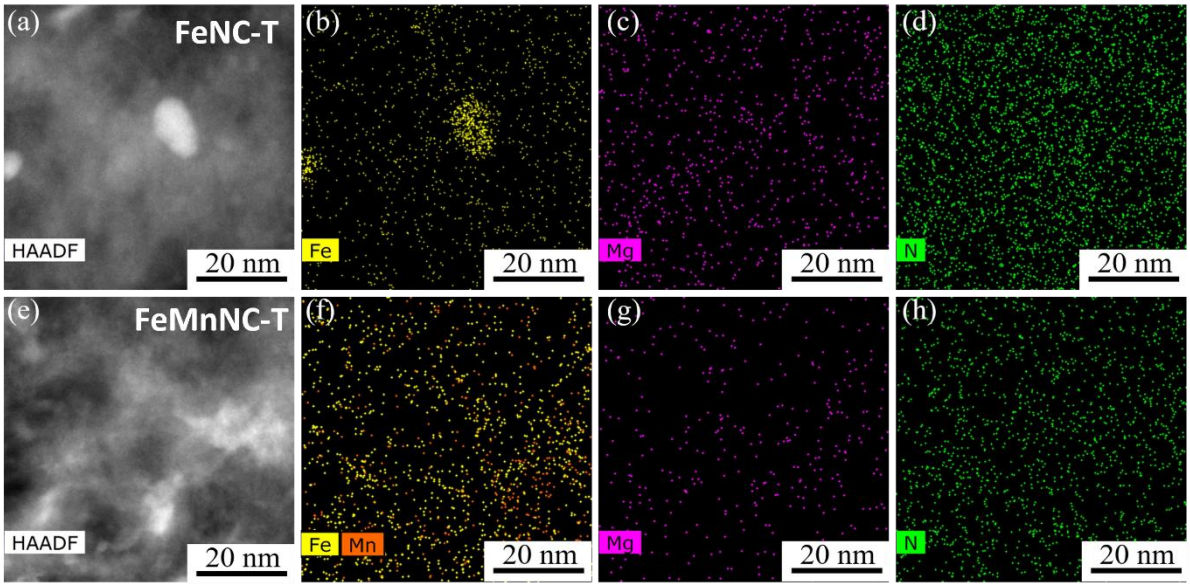

Figure 1. (a, e) HAADF-STEM images and (b, c, d, f, g, h) EDX mapping images of (a-d) FeNC-T and (e-h) FeMnNC-T catalysts.

X-ray diffraction (XRD) analysis (Figure 2a) was conducted to determine the crystallographic structure and composition of the catalyst materials. The XRD patterns reveal a broad, sharp-peaked signal at 26° (2θ), suggesting a disordered carbon structure. The non-acid treated sample includes peaks indexed to MgO (PDF 00-045-0946) and magnesium cyanamide (PDF 00-051-0540), with a crystalline particle size of 4–5 nm obtained from the integrated width of the peaks, both of which are partly responsible for the increased porosity of the materials. It has been observed that in the presence of a nitrogen source (DCDA, melamine etc.) and inorganic templating agent nanoparticles of cyanamide can be formed in situ at above 400 °C [38,39]. We also observed the XRD peaks ascribed to Fe and/or Mn carbides in the non-acid treated FeMnNC-T, however it is not possible to assign them to a specific carbide, it is most likely carbide(s) consisting of both Fe and Mn. After the acid-treatment, the FeMnNC-T and FeNC-T samples are much more amorphous consisting mostly of carbon with a small amount of little carbide and metal crystallites. The FeNC-T catalyst shows peaks indexed to Fe_3C (PDF 00-034-0001) and Fe (PDF 04-007-9753). However, no peaks indexed to MgO or any other Mg species can be observed in the either of the acid treated materials, evidencing the successful removal of the sacrificial template nanoparticles. Even though, some Mg is left in the materials, presumably coordinated with nitrogen in atomically dispersed form.

To ascertain the specific surface area (SSA) and pore size distribution (PSD) of the prepared electrocatalysts, N_2 physisorption analysis was employed. Type III isotherms were

determined for the different electrocatalysts (inset to Figure 2b). As seen from the PSD graph (Figure 2b) the materials contain both micro- and mesopores with a wide size range. Most of the mesopores have diameters around 3 to 4 nm, but larger mesopores are also present, increasing the available pore volume. DCDA, in addition to introducing the necessary nitrogen moieties into the carbon framework, also acts as a structure directing agent by forming g-C_3N_4 during pyrolysis [40]. The carbon precursor is trapped between the layered g-C_3N_4 structure, which is decomposed into reactive nitrogen gases and is responsible for creating porosity in the untemplated FeNC catalyst [41]. The introduction of the Mg-based sacrificial template resulted in a two-fold increase in the SSA value of the FeNC-T and FeMnNC-T materials vs. FeNC by creating additional micro- and mesoporosity (see Table 2). When subjected to temperatures of around 200 °C, $Mg(CH_3COO)_2$ is decomposed and forms nanosized particles of MgO and $MgCN_2$ that are responsible for creating the additional porosity after the nanoparticles are dissolved [27]. Studies have shown that the morphology can significantly differ based on the mass ratios of carbon precursor to MgO, as well as the type of precursors and synthesis conditions such as the pyrolysis temperature [27,42]. Such hierarchical porosity facilitates the mass-transfer of reactants to the active sites, enhancing the overall reaction rate [20]. Simultaneously, the higher porosity leads to an increase in the proportion of electrochemically available active sites, thus further improving the ORR activity of the catalyst. For oxygen and water to be effectively transported in the cathode layer, it is also necessary for macropores to be present. However, the larger macropores cannot be detected using nitrogen sorption isotherms, due to the upper limit of detection around 100 nm for this method. Multiple studies have also reported the synthesis of PGM-free catalysts with optimized porous structures, which have demonstrated improved ORR activities, highlighting the importance of the carbon structure in improving fuel cell performance [21,22,43].

Table 2. Specific surface area (S_{DFT}), surface area from micro-and mesopores (S_{micro} and S_{meso}), micropore volume (V_{μ}) and total pore volume (V_{tot}) of the catalysts.

Catalyst	S_{DFT} ($m^2\ g^{-1}$)	S_{micro} ($m^2\ g^{-1}$)	S_{meso} ($m^2\ g^{-1}$)	V_{μ} ($cm^3\ g^{-1}$)	V_{tot} ($cm^3\ g^{-1}$)
FeNC	299	152	147	0.06	0.76
FeNC-T	653	330	323	0.17	1.08
FeMnNC-T	620	318	302	0.16	0.99

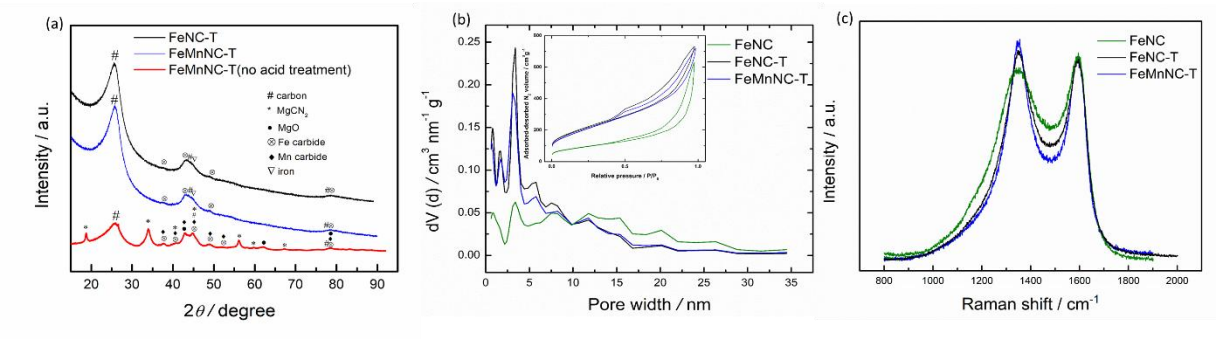

Figure 2. (a) XRD patterns, (b) pore size distribution (with the respective N_2 physisorption isotherms shown in the inset), and (c) Raman spectra of the various catalyst materials.

Figure 2c shows the first-order Raman spectra of the catalysts, normalized to the intensity of the G band. It is important to note that the often-applied I_D/I_G Raman band ratio is typically used to assess the structural imperfection of graphene family materials. However, in heterogenous disordered carbons, the apparent peak labeled as G is a combination of the G and D2 peaks, as such the I_D/I_G ratio is not a reliable descriptor of structural disorder in these materials [44,45]. To assess the extent of structural disorder in the catalyst materials, Table S1 presents the full width at half-maximum (FWHM) of the D1 and G+D2 bands, as well as the I_D/I_{G+D2} ratio. The widths of the respective bands provide indications of structural disorder in defective carbon materials [46]. Based on Figure 2c and the W_{D1} presented in Table S1, it can be concluded that all the catalysts exhibit a high degree of disorder, consistent with the XRD results. The catalysts prepared with the addition of the sacrificial template show a slightly higher level of graphitization. In addition, the Raman spectroscopy analysis revealed an interesting finding, when compared to the purely iron-doped material, the inclusion of manganese seems to promote the graphitization of carbon. Similar findings have been previously published [15,20], as such using Mn to achieve a higher degree of graphitization represents a promising avenue to design PGM-free catalysts with improved durability. Previous studies have demonstrated that a higher degree of graphitization is advantageous for ORR catalysts by improving carbon corrosion resistance [8]. Unlike in Pt/C catalysts, where carbon material primarily functions as a conductive support, carbon in PGM-free catalysts covalently interacts with the active sites. If the carbon material undergoes corrosion or degradation, it can have severe consequences for the performance of the catalyst via the detachment of the M-N_x sites from the carbon planes, resulting in the loss of electrocatalytic activity [20]. Therefore, a highly graphitized carbon support can enhance the overall stability of the catalyst, but it may come at the expense of reducing the number of defects available for anchoring the M-N_x sites. Balancing the density of active sites with the

degree of graphitization in the carbon catalyst is crucial for optimizing catalyst performance [20].

X-ray photoelectron spectroscopy (XPS) analysis was conducted to assess the surface elemental composition of the catalyst materials. The XPS survey and the detailed N 1s spectra are displayed in Figure S4. The catalysts' surfaces contained carbon, nitrogen, oxygen, iron, and manganese (Table 3). FeNC-T had a higher content of both nitrogen and oxygen, but FeMnNC-T showed a slightly higher amount of metals (Fe+Mn) on the surface. Deconvolution of the N 1s XPS spectra is shown in Figure S4b and d. A similar percentage of M-N_x species of around 19-21% (relative to the total N content) can be detected on the surface for both catalysts. Even though nitrogen moieties are considered not to be very ORR-active in acidic media, it has been shown that highly basic N-groups can enhance the TOF value of nearby M-N_x sites [47,48]. Both catalysts display a dominant pyridinic-N peak, however, there are slight differences compared to the other N-groups (Table S2). FeMnNC-T contains slightly less hydrogenated-N and graphitic-N species compared to FeNC-T, while containing more imines.

Table 3. Surface elemental composition of the catalyst materials (at%) by XPS analysis.

Catalyst	C	N	O	Fe	Mn
FeNC-T	85.0	7.3	7.7	0.3	-
FeMnNC-T	88.3	5.0	6.2	0.3	0.2

Microwave plasma-atomic emission spectrometry (MP-AES) (Table S3) and SEM-EDX (Table S4) analysis was used to determine the total metal content. The bulk metal content in these materials is relatively high (around 5-8 wt%), the high iron concentration leads to both agglomerated species as iron carbide and iron nanoparticles in addition to atomically dispersed Fe-N_x sites. The FeNC catalysts contains a significantly higher amount of metal compared to both FeNC-T and FeMnNC-T. We presume the difference in metal content is due to the porous structure, as the inclusion of the Mg acetate in the synthesis increases the surface area and porosity of the catalyst, thereby providing easier access of acid solution to the metal-containing nanoparticles during the leaching procedure. Interestingly, all of the manganese seems to be dispersed with no large agglomerates. In most cases, simply increasing the metal content without careful consideration or optimization of the synthesis procedure leads to greater production of metal clusters in the form of nanoparticles or carbides instead of M-N_x sites. It has been shown that carbon substrates with larger surface areas are beneficial in facilitating the dispersion of Fe atoms at high metal concentrations

[47,49,50], which further highlights the benefit of using a sacrificial template to increase the SSA and avoid agglomeration of the metal.

3.2 Electrochemical characterization

RDE setup was used for the determination of the catalysts' ORR electrocatalytic activity in 0.5 M H_2SO_4 electrolyte solution. The linear sweep voltammograms (LSVs) of different catalyst materials are displayed in Figure 3 and the cyclic voltammograms recorded in O_2-free solution in Figure S5. All of the electrocatalysts prepared in this work displayed similar ORR activities when comparing their onset potentials (E_{onset}) and half-wave potentials ($E_{1/2}$) (Table S5). FeNC-T and FeMnNC-T achieved the $E_{1/2}$ value of 0.75 V vs. RHE, which is 67 mV lower than that of a commercial Pt/C catalyst. Despite the much higher bulk metal content of the FeNC catalyst, the ORR activity remained very similar, indicating that a significant portion of the iron is not coordinated to nitrogen and is susceptible to agglomeration into nanoparticles during the thermal treatment. Furthermore, many Fe-N_x sites could be buried deep in the micropores of the catalyst and thereby inaccessible to O_2, resulting from the much lower mesoporosity for this catalyst.

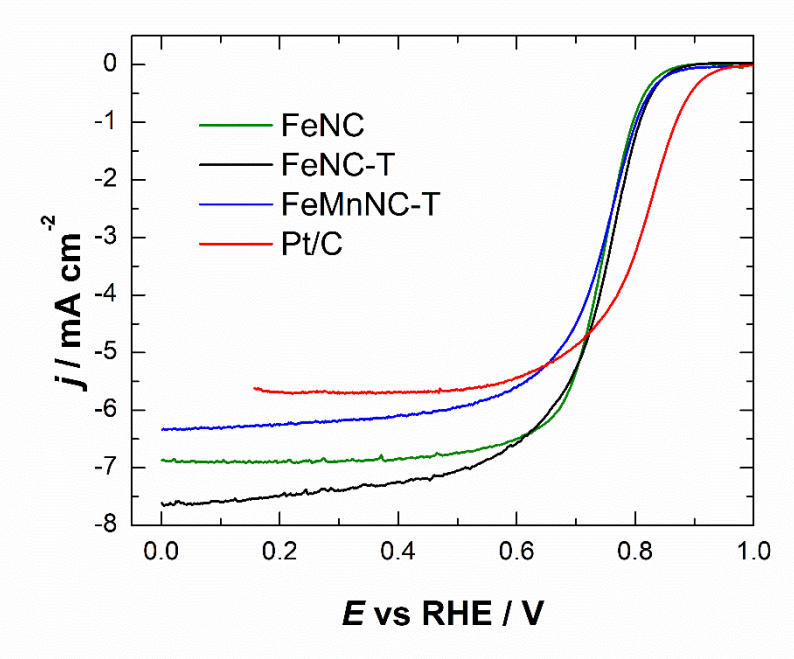

Figure 3. Comparison of RDE voltammetry curves for ORR on various PGM-free catalysts and commercial Pt/C in O_2-saturated 0.5 M H_2SO_4 solution at 1900 rpm. ν = 10 mV s^{-1}.

The number of electrons transferred per O_2 molecule for the iron-containing catalysts during the ORR process is about 3.8 (Table S5), obtained from the K-L analysis of RDE data (Figure S6). The bimetallic FeMnNC-T has a slightly higher *n* value (3.9). A significant issue with

FeNC catalysts is the occurrence of Fenton reactions between Fe^{2+} ions and hydrogen peroxide (H_2O_2), which is a byproduct of ORR. The oxygen-containing radicals generated through the Fenton reactions can cause the degradation of organic components such as ionomers and membranes, and even the catalysts themselves [51]. When comparing the peroxide yields determined by RRDE method (Figure 4), it is observed that the solely iron-doped carbon material exhibits lower selectivity for $4e^-$ reduction, leading to higher peroxide yields (12-15%). On the other hand, FeMnNC-T catalyst mainly follows a $4e^-$ ORR pathway, with peroxide yields below 10% (see Figure 4c). Although, the obtained peroxide percentage yield could be influenced by the catalyst layer thickness, since some research has shown that higher loadings can lead to the underestimation of the H_2O_2 yield. The high loading (0.8 mg cm^{-2}) used in this work could interfere with the diffusion of the peroxide, leading to its decomposition before reaching the ring electrode [52]. Still, other studies have indicated that the detected H_2O_2 is not always heavily influenced by the catalyst layer thickness [53]. It should be also pointed out that the peroxide yield is likely to be quite different transitioning from half-cell to MEA tests in a fuel cell device, which could impede the application of the RRDE results [54].

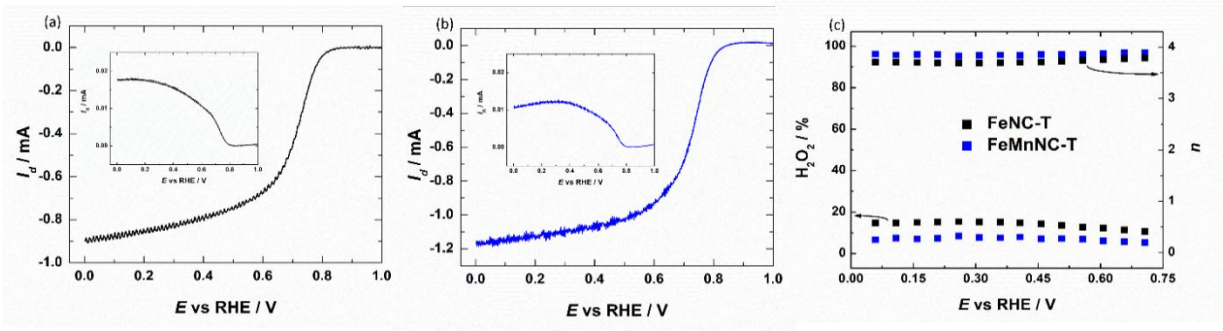

Figure 4. RRDE voltammetry curves for ORR in O_2- saturated 0.5 M H_2SO_4 solution at 960 rpm (insets show the respective ring currents) for (a) FeNC-T and (b) FeMnNC-T catalysts; (c) percentage yield of H_2O_2 formation and the *n* value as a function of potential. ν = 10 mV s^{-1}.

Stability is one of the main challenges associated with PGM-free catalyst in acidic media. Precise explanations concerning the processes of degradation are currently being actively discussed in the literature, as many different viewpoints have emerged regarding the potential failure mechanisms. In a recent review by Shao et al. [55] the main contributors to the drop in performance of PGM-free catalysts were outlined as follows: micropore flooding, protonation and adsorption of anions at active sites, demetallation, and carbon oxidation.

In this work, as demonstrated in Figure 5, there is a significant drop in the ORR activity during the first 1000 potential cycles, after which the rate of decrease slows down. After

10000 CVs, for the FeNC-T catalyst, the $E_{1/2}$ value shifted negative by 76 mV, and for FeMnNC-T the $\Delta E_{1/2}$ was -66 mV. The initial rapid decrease can be attributed to the demetallation of M-N_x sites, followed by more gradual decrease related to carbon corrosion. Similar trends have been found in multiple studies, where the initial stage is followed by the second stage where the catalyst experiences a gradual decrease, persisting throughout its entire lifespan [8,56,57]. For the untemplated FeNC catalyst, the decrease in activity is quite rapid, eventually the $E_{1/2}$ value shifted by 95 mV in negative direction. Raman spectroscopy studies confirmed the smaller degree of graphitization for FeNC, which can lead to more significant carbon corrosion and is likely behind the larger decrease in the ORR performance. The presence of imperfect graphitic carbon shells surrounding the metallic particles could offer an additional explanation for the loss of electrocatalytic activity, due to allowing the acidic electrolyte to reach the metal particles causing additional demetallation [8]. This might be most significant in the case of FeNC catalyst, where the carbon is more disordered, and the overall iron content is very high. It should be highlighted that degradation pathways are often interconnected, affecting both the active sites at the atomic level and the properties of the electrode layer at the macroscale and mesoscale. For example, oxidation of carbon results in degradation of carbon structure, followed by demetallation of active sites [55].

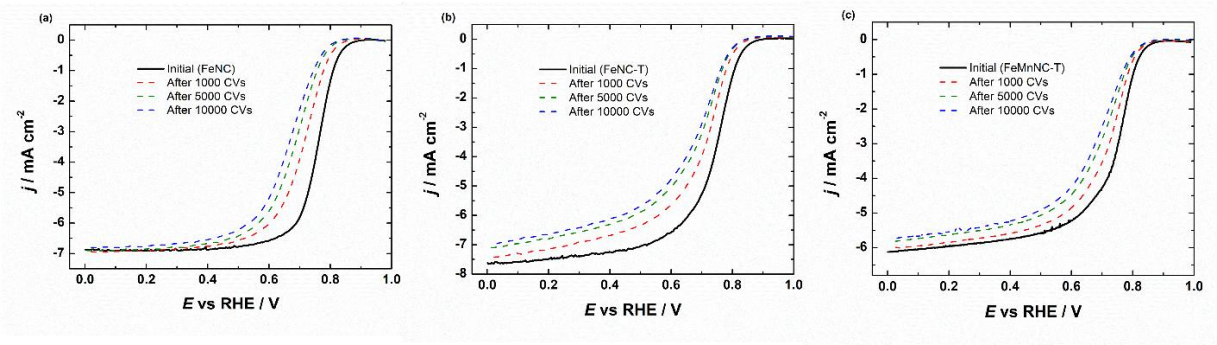

Figure 5. RDE voltammetry curves for O_2 reduction before and after repetitive potential cycles for (a) FeNC; (b) FeNC-T, and (c) FeMnNC-T catalysts (ω =1900 rpm and ν = 10 mV s^{-1}).

3.3 Proton exchange membrane fuel cell measurements

Next, the electrocatalysts were studied in MEAs under H_2-O_2 conditions to investigate the fuel cell performance at low voltage. The high current density region is constrained by mass transport and cannot be explored using RDE due to the low concentration of O_2 that can be dissolved in the electrolyte [58]. Both FeNC-T and FeMnNC-T catalysts showed promising fuel cell performance with peak power densities (P_{max}) of 514 and 334 mW cm^{-2}, respectively (Figure 6). The MEA prepared with FeNC demonstrated a discernibly lower

performance, especially at lower voltages, achieving only a moderate P_{max} value of 188 mW cm^{-2}. The higher performance of the catalysts prepared with the sacrificial template at higher current densities can be explained by the improved transport of reactants and products to and from the active sites due to the increased mesoporosity in these catalysts, which could expose additional active sites at three-phase boundaries in the catalyst layer. Several studies have shown that achieving the optimal carbon structure is crucial for PGM-free catalyst materials because of the thick catalyst layers due to the high metal site loading needed [59,60]. A loading of 4 mg cm^{-2} results in a thickness of about 100 µm [20,61,62], compared to Pt/C cathodes that are approximately an order of magnitude thinner [63]. Because of the lower thickness of the catalyst layer, the commercial Pt-based cathode is able to achieve much higher current densities (Figure 6). Therefore, even though a hierarchical porous structure that facilitates efficient O_2 transport and even ionomer coverage is helpful in increasing the performance for PGM-free catalyst materials, further improvements in the catalyst design are needed to match the performance of PGM-based cathodes.

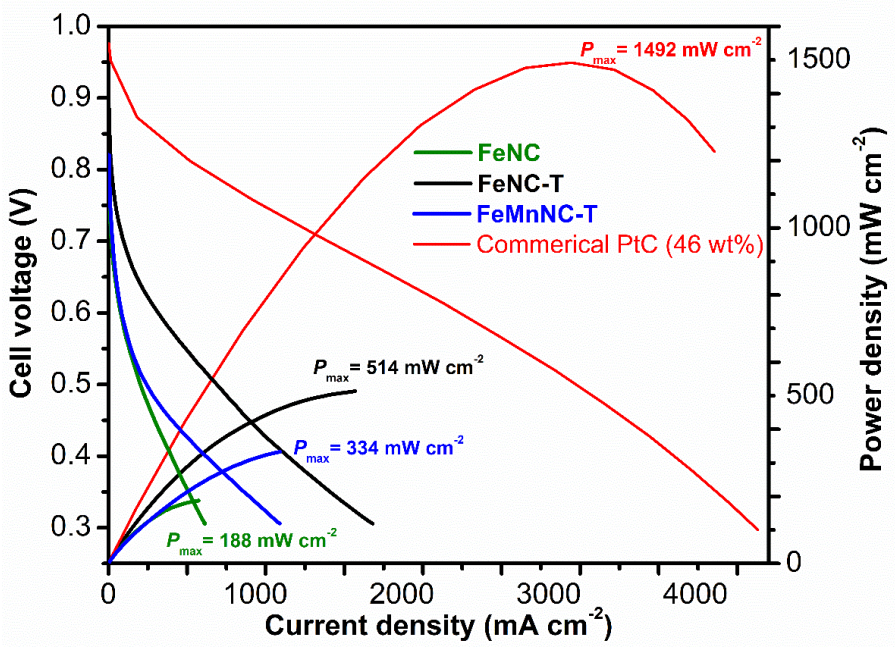

Figure 6. Polarization and power density curves for the PGM-free electrocatalysts with H_2-O_2 PEMFC and 100% relative humidity at 80 °C, 2 bar backpressure, and 0.3 NLPM flow rate of gases on both the anode and cathode side. Cathode loading of 4 mg cm^{-2} (for PGM-free catalysts) or 0.25 mg_{Pt} cm^{-2} (for PGM catalyst).

It is less clear why the bimetallic FeMnNC-T catalyst shows a decreased PEMFC performance. It cannot be explained by the difference in the carbon material morphology, as the STEM and N_2 adsorption/desorption measurements show that this is very similar for these two catalysts. A plausible explanation could be that due to slightly different surface

composition of the bimetallic catalyst, evidenced by the XPS analysis and EDX mapping, and the higher degree of graphitization, the ionomer interaction with carbon support is different and this alters the ionomer distribution. If the ionomer forms a closer interaction with the catalyst surface, its more homogeneous distribution across the electrode will be achieved [64]. To improve the FC performance, the cathode ink and MEA preparation was optimized using FeNC-T catalyst and the same formulation were used with the other catalysts in order to lower the number of variables. However, due to the different properties of FeMnNC-T, it may require a slightly different ink formulation to obtain the optimal performance. In order to confirm this theory, a detailed investigation of the ionomer distribution and porosity within the catalyst layer would be needed, which is outside the scope of this work.

4. Conclusions

In this study, we have addressed the challenges associated with PEMFCs by exploring alternative mesoporous PGM-free catalysts. By incorporating iron and manganese as transition metal dopants, we aimed to enhance the ORR activity while mitigating the undesired Fenton reactions. The observed improvements in the stability under harsh corrosive conditions highlight the potential of the addition of Mn in increasing the durability of such carbon-based catalysts. Our investigation emphasizes the critical role of hierarchically porous structures, particularly in MEAs, to enhance the electrocatalytic performance. The catalysts prepared with sustainable synthesis procedure using magnesium acetate as the template precursor, showed much higher peak power density values, compared to the less mesoporous material, demonstrating the importance of hierarchically porous structures in PGM-free catalysts in PEMFC conditions.

CRediT authorship contribution statement

Kaarel Kisand: Conceptualization, Investigation, Methodology, Visualization, Formal Analysis, Writing - Original draft preparation, Writing - Review & Editing. **Ave Sarapuu**: Supervision, Methodology, Writing - Review & Editing. **Srinu Akula:** Investigation, Formal analysis, Writing - Review & Editing. **Arvo Kikas:** Investigation, Formal analysis, Writing - Review & Editing. **Alexey Treshchalov**: Investigation, Methodology, Writing - Review & Editing. **Maike Käärik:** Investigation, Methodology, Formal analysis. **Helle-Mai Piirsoo**: Investigation, Methodology, Formal analysis. **Jekaterina Kozlova:** Investigation, Formal analysis, Writing - Review & Editing. **Jaan Aruväli:** Investigation, Formal analysis. **Jaan**

Leis: Resources, Funding acquisition, Writing - Review & Editing. **Vambola Kisand:** Resources, Funding acquisition. **Kaupo Kukli:** Resources, Funding acquisition, Writing - Review & Editing. **Ghenwa El Chawich:** Investigation, Formal analysis. **Frédéric Jaouen:** Resources, Methodology, Funding acquisition, Writing - Review & Editing. **Sara Cavaliere:** Resources, Funding acquisition, Writing - Review & Editing. **Kaido Tammeveski:** Supervision, Resources, Methodology, Funding acquisition, Writing - Review & Editing.

Data availability

Data will be made available on request.

Declaration of competing interest

The authors declare that they have no known competing financial interests or personal relationships that could have appeared to influence the work reported in this paper.

Acknowledgments

The present work was financially supported by the Estonian Research Council (grants PRG723, PRG753, and PRG1509) and the M-ERA.Net project "C-MOF.cell" (SLTKT20445). This research was also supported by the Estonian Ministry of Education and Research (TK210, Centre of Excellence in Sustainable Green Hydrogen and Energy Technologies). Many thanks to Viru Keemia Grupp for providing us with Honeyol.

References

[1] Y. Wang, D.F. Ruiz Diaz, K.S. Chen, Z. Wang, X.C. Adroher, Materials, technological status, and fundamentals of PEM fuel cells – A review, Mater.Today 32 (2020) 178–203. https://doi.org/10.1016/j.mattod.2019.06.005.

[2] L. Osmieri, J. Park, D.A. Cullen, P. Zelenay, D.J. Myers, K.C. Neyerlin, Status and challenges for the application of platinum group metal-free catalysts in proton-exchange membrane fuel cells, Curr. Opin. Electrochem. 25 (2021) 100627. https://doi.org/10.1016/j.coelec.2020.08.009.

[3] L. Jiao, J. Li, L.L. Richard, Q. Sun, T. Stracensky, E. Liu, M.T. Sougrati, Z. Zhao, F. Yang, S. Zhong, H. Xu, S. Mukerjee, Y. Huang, D.A. Cullen, J.H. Park, M. Ferrandon, D.J. Myers, F. Jaouen, Q. Jia, Chemical vapour deposition of Fe–N–C oxygen reduction catalysts with full utilization of dense Fe–N4 sites, Nat. Mater. 20 (2021) 1385–1391. https://doi.org/10.1038/s41563-021-01030-2.

[4] X. Wan, X. Liu, Y. Li, R. Yu, L. Zheng, W. Yan, H. Wang, M. Xu, J. Shui, Fe–N–C electrocatalyst with dense active sites and efficient mass transport for high-performance

proton exchange membrane fuel cells, Nat. Catal. 2 (2019) 259–268. https://doi.org/10.1038/s41929-019-0237-3.
[5] A. Mehmood, J. Pampel, G. Ali, H.Y. Ha, F. Ruiz-Zepeda, T.-P. Fellinger, Facile Metal Coordination of Active Site Imprinted Nitrogen Doped Carbons for the Conservative Preparation of Non-Noble Metal Oxygen Reduction Electrocatalysts, Adv. Energy Mater. 8 (2018) 1701771. https://doi.org/10.1002/aenm.201701771.
[6] A. Sarapuu, J. Lilloja, S. Akula, J.H. Zagal, S. Specchia, K. Tammeveski, Recent Advances in Non-Precious Metal Single-Atom Electrocatalysts for Oxygen Reduction Reaction in Low-Temperature Polymer-Electrolyte Fuel Cells, ChemCatChem 15 (2023) e202300849. https://doi.org/10.1002/cctc.202300849.
[7] S.H. Al-Hilfi, X. Jiang, J. Heuer, S. Akula, K. Tammeveski, G. Hu, J. Yang, H.I. Wang, M. Bonn, K. Landfester, K. Müllen, Y. Zhou, Single-Atom Catalysts through Pressure-Controlled Metal Diffusion, J. Am. Chem. Soc. (2024). https://doi.org/10.1021/jacs.4c03066.
[8] K. Kumar, P. Gairola, M. Lions, N. Ranjbar Sahraie, M. Mermoux, L. Dubau, A. Zitolo, F. Jaouen, F. Maillard, Physical and Chemical Considerations for Improving Catalytic Activity and Stability of Non-Precious-Metal Oxygen Reduction Reaction Catalysts, ACS Catal. 8 (2018) 11264–11276. https://doi.org/10.1021/acscatal.8b02934.
[9] Y. Hu, J.O. Jensen, W. Zhang, L.N. Cleemann, W. Xing, N.J. Bjerrum, Q. Li, Hollow Spheres of Iron Carbide Nanoparticles Encased in Graphitic Layers as Oxygen Reduction Catalysts, Angew. Chem. Int. Ed. 53 (2014) 3675–3679. https://doi.org/10.1002/anie.201400358.
[10] Z.-Y. Wu, X.-X. Xu, B.-C. Hu, H.-W. Liang, Y. Lin, L.-F. Chen, S.-H. Yu, Iron Carbide Nanoparticles Encapsulated in Mesoporous Fe-N-Doped Carbon Nanofibers for Efficient Electrocatalysis, Angew. Chem. Int. Ed 54 (2015) 8179–8183. https://doi.org/10.1002/anie.201502173.
[11] Y. Kumar, E. Kibena-Põldsepp, S. Akula, J. Kozlova, A. Kikas, J. Aruväli, V. Kisand, K. Kukli, K. Tammeveski, The effect of additional nitrogen source on iron phthalocyanine-based nanocarbon catalysts for oxygen reduction reaction in acidic media, Electrochem. Commun. 157 (2023) 107623. https://doi.org/10.1016/j.elecom.2023.107623.
[12] K. Kumar, L. Dubau, F. Jaouen, F. Maillard, Review on the Degradation Mechanisms of Metal-N-C Catalysts for the Oxygen Reduction Reaction in Acid Electrolyte: Current Understanding and Mitigation Approaches, Chem. Rev. (2023). https://doi.org/10.1021/acs.chemrev.2c00685.
[13] S.T. Thompson, A.R. Wilson, P. Zelenay, D.J. Myers, K.L. More, K.C. Neyerlin, D. Papageorgopoulos, ElectroCat: DOE's approach to PGM-free catalyst and electrode R&D, Solid State Ionics 319 (2018) 68–76. https://doi.org/10.1016/j.ssi.2018.01.030.
[14] K. Liu, Z. Qiao, S. Hwang, Z. Liu, H. Zhang, D. Su, H. Xu, G. Wu, G. Wang, Mn- and N- doped carbon as promising catalysts for oxygen reduction reaction: Theoretical prediction and experimental validation, Appl. Catal. B 243 (2019) 195–203. https://doi.org/10.1016/j.apcatb.2018.10.034.
[15] J. Li, M. Chen, D.A. Cullen, S. Hwang, M. Wang, B. Li, K. Liu, S. Karakalos, M. Lucero, H. Zhang, C. Lei, H. Xu, G.E. Sterbinsky, Z. Feng, D. Su, K.L. More, G. Wang, Z. Wang, G. Wu, Atomically dispersed manganese catalysts for oxygen reduction in proton-exchange membrane fuel cells, Nat. Catal. 1 (2018) 935–945. https://doi.org/10.1038/s41929-018-0164-8.
[16] Z. Chen, X. Liao, C. Sun, K. Zhao, D. Ye, J. Li, G. Wu, J. Fang, H. Zhao, J. Zhang, Enhanced performance of atomically dispersed dual-site Fe-Mn electrocatalysts through

cascade reaction mechanism, Appl. Catal. B 288 (2021) 120021. https://doi.org/10.1016/j.apcatb.2021.120021.
[17] S. Huang, Z. Qiao, P. Sun, K. Qiao, K. Pei, L. Yang, H. Xu, S. Wang, Y. Huang, Y. Yan, D. Cao, The strain induced synergistic catalysis of FeN4 and MnN3 dual-site catalysts for oxygen reduction in proton- /anion- exchange membrane fuel cells, Appl. Catal. B 317 (2022) 121770. https://doi.org/10.1016/j.apcatb.2022.121770.
[18] K. Kisand, A. Sarapuu, D. Danilian, A. Kikas, V. Kisand, M. Rähn, A. Treshchalov, M. Käärik, M. Merisalu, P. Paiste, J. Aruväli, J. Leis, V. Sammelselg, S. Holdcroft, K. Tammeveski, Transition metal-containing nitrogen-doped nanocarbon catalysts derived from 5-methylresorcinol for anion exchange membrane fuel cell application, J. Coll. Int. Sci. 584 (2021) 263–274. https://doi.org/10.1016/j.jcis.2020.09.114.
[19] S. Ratso, I. Kruusenberg, A. Sarapuu, M. Kook, P. Rauwel, R. Saar, J. Aruväli, K. Tammeveski, Electrocatalysis of oxygen reduction on iron- and cobalt-containing nitrogen-doped carbon nanotubes in acid media, Electrochim. Acta 218 (2016) 303–310. https://doi.org/10.1016/j.electacta.2016.09.119.
[20] Y. He, S. Liu, C. Priest, Q. Shi, G. Wu, Atomically dispersed metal–nitrogen–carbon catalysts for fuel cells: advances in catalyst design, electrode performance, and durability improvement, Chem. Soc. Rev. 49 (2020) 3484–3524. https://doi.org/10.1039/C9CS00903E.
[21] K. Kisand, A. Sarapuu, J.C. Douglin, A. Kikas, A. Treshchalov, M. Käärik, H.-M. Piirsoo, P. Paiste, J. Aruväli, J. Leis, V. Kisand, A. Tamm, D.R. Dekel, K. Tammeveski, Templated Nitrogen-, Iron-, and Cobalt-Doped Mesoporous Nanocarbon Derived from an Alkylresorcinol Mixture for Anion-Exchange Membrane Fuel Cell Application, ACS Catal. 12 (2022) 14050–14061. https://doi.org/10.1021/acscatal.2c03683.
[22] S. Lee, D.-H. Kwak, S.-B. Han, Y.-W. Lee, J.-Y. Lee, I.-A. Choi, H.-S. Park, J.-Y. Park, K.-W. Park, Bimodal Porous Iron/Nitrogen-Doped Highly Crystalline Carbon Nanostructure as a Cathode Catalyst for the Oxygen Reduction Reaction in an Acid Medium, ACS Catal. 6 (2016) 5095–5102. https://doi.org/10.1021/acscatal.5b02721.
[23] S.H. Lee, J. Kim, D.Y. Chung, J.M. Yoo, H.S. Lee, M.J. Kim, B.S. Mun, S.G. Kwon, Y.-E. Sung, T. Hyeon, Design Principle of Fe–N–C Electrocatalysts: How to Optimize Multimodal Porous Structures?, J. Am. Chem. Soc. 141 (2019) 2035–2045. https://doi.org/10.1021/jacs.8b11129.
[24] J. Lilloja, M. Mooste, E. Kibena-Põldsepp, A. Sarapuu, A. Kikas, V. Kisand, M. Käärik, J. Kozlova, A. Treshchalov, P. Paiste, J. Aruväli, J. Leis, A. Tamm, S. Holdcroft, K. Tammeveski, Cobalt-, iron- and nitrogen-containing ordered mesoporous carbon-based catalysts for anion-exchange membrane fuel cell cathode, Electrochim. Acta 439 (2023) 141676. https://doi.org/10.1016/j.electacta.2022.141676.
[25] A. Serov, M.H. Robson, K. Artyushkova, P. Atanassov, Templated non-PGM cathode catalysts derived from iron and poly(ethyleneimine) precursors, Appl. Catal. B 127 (2012) 300–306. https://doi.org/10.1016/j.apcatb.2012.08.040.
[26] A. Serov, K. Artyushkova, P. Atanassov, Fe-N-C Oxygen Reduction Fuel Cell Catalyst Derived from Carbendazim: Synthesis, Structure, and Reactivity, Adv. Energy Mater. 4 (2014) 1301735. https://doi.org/10.1002/aenm.201301735.
[27] T. Morishita, T. Tsumura, M. Toyoda, J. Przepiórski, A.W. Morawski, H. Konno, M. Inagaki, A review of the control of pore structure in MgO-templated nanoporous carbons, Carbon 48 (2010) 2690–2707. https://doi.org/10.1016/j.carbon.2010.03.064.
[28] B. Koyuturk, E. M. Farber, F. E. Wagner, T.-P. Fellinger, D. Eisenberg, A simple decagram-scale synthesis of an atomically dispersed, hierarchically porous Fe–N–C catalyst for acidic ORR, J. Mater. Chem. A 10 (2022) 19859–19867. https://doi.org/10.1039/D2TA00925K.

[29] D. Eisenberg, P. Prinsen, N. J. Geels, W. Stroek, N. Yan, B. Hua, J.-L. Luo, G. Rothenberg, The evolution of hierarchical porosity in self-templated nitrogen-doped carbons and its effect on oxygen reduction electrocatalysis, RSC Adv. 6 (2016) 80398–80407. https://doi.org/10.1039/C6RA16606G.
[30] N. Díez, M. Sevilla, A.B. Fuertes, Synthesis strategies of templated porous carbons beyond the silica nanocasting technique, Carbon 178 (2021) 451–476. https://doi.org/10.1016/j.carbon.2021.03.029.
[31] M. Inagaki, S. Kobayashi, F. Kojin, N. Tanaka, T. Morishita, B. Tryba, Pore structure of carbons coated on ceramic particles, Carbon 42 (2004) 3153–3158. https://doi.org/10.1016/j.carbon.2004.07.029.
[32] A. J. Bard, L. R. Faulkner, Electrochemical Methods: Fundamentals and Applications, 2nd ed., New York: Wiley, 2001; pp 340-344.
[33] S. Gottesfeld, I.D. Raistrick, S. Srinivasan, Oxygen Reduction Kinetics on a Platinum RDE Coated with a Recast Nafion Film, J. Electrochem. Soc. 134 (1987) 1455. https://doi.org/10.1149/1.2100689.
[34] Accelerated Stress Test and Polarization Curve Protocols for PEMFCs. (U.S. Department of Energy Hydrogen and Fuel Cells Technology Office, 2013). https://www.energy.gov/eere/fuelcells/articles/fuel-cell-tech-team-accelerated-stress-test-and-polarization-curve
[35] L. Osmieri, D.A. Cullen, H.T. Chung, R.K. Ahluwalia, K.C. Neyerlin, Durability evaluation of a Fe–N–C catalyst in polymer electrolyte fuel cell environment via accelerated stress tests, Nano Energy 78 (2020) 105209. https://doi.org/10.1016/j.nanoen.2020.105209.
[36] R.K. Ahluwalia, X. Wang, L. Osmieri, J.-K. Peng, C.F. Cetinbas, J. Park, D.J. Myers, H.T. Chung, K.C. Neyerlin, Stability of Atomically Dispersed Fe–N–C ORR Catalyst in Polymer Electrolyte Fuel Cell Environment, J. Electrochem. Soc. 168 (2021) 024513. https://doi.org/10.1149/1945-7111/abe34c.
[37] G. Wu, M.A. Nelson, N.H. Mack, S. Ma, P. Sekhar, F.H. Garzon, P. Zelenay, Titanium dioxide-supported non-precious metal oxygen reduction electrocatalyst, Chem. Commun. 46 (2010) 7489–7491. https://doi.org/10.1039/C0CC03088K.
[38] X.-X. Peng, Y.-Q. Lu, L.-L. Zhou, T. Sheng, S.-Y. Shen, H.-G. Liao, L. Huang, J.-T. Li, S.-G. Sun, Graphitized porous carbon materials with high sulfur loading for lithium-sulfur batteries, Nano Energy 32 (2017) 503–510. https://doi.org/10.1016/j.nanoen.2016.12.060.
[39] G. Yang, H. Han, T. Li, C. Du, Synthesis of nitrogen-doped porous graphitic carbons using nano-CaCO3 as template, graphitization catalyst, and activating agent, Carbon 50 (2012) 3753–3765. https://doi.org/10.1016/j.carbon.2012.03.050.
[40] C. Hu, Y. Zhou, R. Ma, Q. Liu, J. Wang, Reactive template synthesis of nitrogen-doped graphene-like carbon nanosheets derived from hydroxypropyl methylcellulose and dicyandiamide as efficient oxygen reduction electrocatalysts, J. Power Sources 345 (2017) 120–130. https://doi.org/10.1016/j.jpowsour.2017.01.124.
[41] Q. Li, D. Xu, X. Ou, F. Yan, Nitrogen-Doped Graphitic Porous Carbon Nanosheets Derived from In Situ Formed g-C3N4 Templates for the Oxygen Reduction Reaction, Chem. Asian J. 12 (2017) 1816–1823. https://doi.org/10.1002/asia.201700586.
[42] W. Chen, Y. Zong, Y. Zhou, W. Lu, Y. Zhang, J. Qian, The nature of MgO precursor decomposition and pore-forming in hard-templating of porous carbon derived from cotton, Coll. Surf. A 571 (2019) 160–167. https://doi.org/10.1016/j.colsurfa.2019.03.091.
[43] S. Akula, M. Mooste, B. Zulevi, S. McKinney, A. Kikas, H.-M. Piirsoo, M. Rähn, A. Tamm, V. Kisand, A. Serov, E.B. Creel, D.A. Cullen, K.C. Neyerlin, H. Wang, M. Odgaard, T. Reshetenko, K. Tammeveski, Mesoporous textured Fe-N-C electrocatalysts

as highly efficient cathodes for proton exchange membrane fuel cells, J. Power Sources 520 (2022) 230819. https://doi.org/10.1016/j.jpowsour.2021.230819.
[44] M. Sforna, M. Zuilen, P. Philippot, Structural characterization by Raman hyperspectral mapping of organic carbon in the 3.46 billion-year-old Apex chert, Western Australia, Geochim. Cosmochim. Acta 124 (2013) 18–33. https://doi.org/10.1016/j.gca.2013.09.031.
[45] A.A.K. King, B.R. Davies, N. Noorbehesht, P. Newman, T.L. Church, A.T. Harris, J.M. Razal, A.I. Minett, A New Raman Metric for the Characterisation of Graphene oxide and its Derivatives, Sci. Rep. 6 (2016) 19491. https://doi.org/10.1038/srep19491.
[46] L.G. Cançado, A. Jorio, E.H.M. Ferreira, F. Stavale, C.A. Achete, R.B. Capaz, M.V.O. Moutinho, A. Lombardo, T.S. Kulmala, A.C. Ferrari, Quantifying Defects in Graphene via Raman Spectroscopy at Different Excitation Energies, Nano Lett. 11 (2011) 3190–3196. https://doi.org/10.1021/nl201432g.
[47] M. Xiao, J. Zhu, L. Ma, Z. Jin, J. Ge, X. Deng, Y. Hou, Q. He, J. Li, Q. Jia, S. Mukerjee, R. Yang, Z. Jiang, D. Su, C. Liu, W. Xing, Microporous Framework Induced Synthesis of Single-Atom Dispersed Fe-N-C Acidic ORR Catalyst and Its in Situ Reduced Fe-N4 Active Site Identification Revealed by X-ray Absorption Spectroscopy, ACS Catal. 8 (2018) 2824–2832. https://doi.org/10.1021/acscatal.8b00138.
[48] J. Li, M.T. Sougrati, A. Zitolo, J.M. Ablett, I.C. Oğuz, T. Mineva, I. Matanovic, P. Atanassov, Y. Huang, I. Zenyuk, A. Di Cicco, K. Kumar, L. Dubau, F. Maillard, G. Dražić, F. Jaouen, Identification of durable and non-durable FeNx sites in Fe–N–C materials for proton exchange membrane fuel cells, Nat. Catal. 4 (2021) 10–19. https://doi.org/10.1038/s41929-020-00545-2.
[49] Z. Yang, Y. Wang, M. Zhu, Z. Li, W. Chen, W. Wei, T. Yuan, Y. Qu, Q. Xu, C. Zhao, X. Wang, P. Li, Y. Li, Y. Wu, Y. Li, Boosting Oxygen Reduction Catalysis with Fe–N4 Sites Decorated Porous Carbons toward Fuel Cells, ACS Catal. 9 (2019) 2158–2163. https://doi.org/10.1021/acscatal.8b04381.
[50] R. Sgarbi, K. Kumar, F. Jaouen, A. Zitolo, E.A. Ticianelli, F. Maillard, Oxygen reduction reaction mechanism and kinetics on M-NxCy and M@N-C active sites present in model M-N-C catalysts under alkaline and acidic conditions, J. Solid State Electrochem. 25 (2021) 45–56. https://doi.org/10.1007/s10008-019-04436-w.
[51] X.X. Wang, V. Prabhakaran, Y. He, Y. Shao, G. Wu, Iron-Free Cathode Catalysts for Proton-Exchange-Membrane Fuel Cells: Cobalt Catalysts and the Peroxide Mitigation Approach, Adv. Mater. 31 (2019) 1805126. https://doi.org/10.1002/adma.201805126.
[52] S. Ünsal, T.J. Schmidt, J. Herranz, Effect of aggregate size and film quality on the electrochemical properties of non-noble metal catalysts in rotating ring disk electrode measurements, Electrochim. Acta 445 (2023) 142024. https://doi.org/10.1016/j.electacta.2023.142024.
[53] F. Jaouen, J.-P. Dodelet, O2 Reduction Mechanism on Non-Noble Metal Catalysts for PEM Fuel Cells. Part I: Experimental Rates of O2 Electroreduction, H2O2 Electroreduction, and H2O2 Disproportionation, J. Phys. Chem. C 113 (2009) 15422–15432. https://doi.org/10.1021/jp900837e.
[54] C. Chen, T.F. Fuller, Modeling of H2O2 formation in PEMFCs, Electrochimica Acta 54 (2009) 3984–3995. https://doi.org/10.1016/j.electacta.2009.02.021.
[55] Y. Shao, J.-P. Dodelet, G. Wu, P. Zelenay, PGM-Free Cathode Catalysts for PEM Fuel Cells: A Mini-Review on Stability Challenges, Adv. Mater. 31 (2019) 1807615. https://doi.org/10.1002/adma.201807615.
[56] J.-Y. Choi, L. Yang, T. Kishimoto, X. Fu, S. Ye, Z. Chen, D. Banham, Is the rapid initial performance loss of Fe/N/C non precious metal catalysts due to micropore

flooding?, Energy Environ. Sci. 10 (2017) 296–305. https://doi.org/10.1039/C6EE03005J.
[57] R. Chenitz, U.I. Kramm, M. Lefèvre, V. Glibin, G. Zhang, S. Sun, J.-P. Dodelet, A specific demetalation of Fe–N4 catalytic sites in the micropores of NC_Ar + NH3 is at the origin of the initial activity loss of the highly active Fe/N/C catalyst used for the reduction of oxygen in PEM fuel cells, Energy Environ. Sci. 11 (2018) 365–382. https://doi.org/10.1039/C7EE02302B.
[58] F. Jaouen, V. Goellner, M. Lefèvre, J. Herranz, E. Proietti, J.P. Dodelet, Oxygen reduction activities compared in rotating-disk electrode and proton exchange membrane fuel cells for highly active FeNC catalysts, Electrochim. Acta 87 (2013) 619–628. https://doi.org/10.1016/j.electacta.2012.09.057.
[59] S. Ratso, N. Ranjbar Sahraie, M.T. Sougrati, M. Käärik, M. Kook, R. Saar, P. Paiste, Q. Jia, J. Leis, S. Mukerjee, F. Jaouen, K. Tammeveski, Synthesis of highly-active Fe–N–C catalysts for PEMFC with carbide-derived carbons, J. Mater. Chem. A 6 (2018) 14663–14674. https://doi.org/10.1039/C8TA02325E.
[60] S. Ratso, M.T. Sougrati, M. Käärik, M. Merisalu, M. Rähn, V. Kisand, A. Kikas, P. Paiste, J. Leis, V. Sammelselg, F. Jaouen, K. Tammeveski, Effect of Ball-Milling on the Oxygen Reduction Reaction Activity of Iron and Nitrogen Co-doped Carbide-Derived Carbon Catalysts in Acid Media, ACS Appl. Energy Mater. 2 (2019) 7952–7962. https://doi.org/10.1021/acsaem.9b01430.
[61] J. Barrio, A. Pedersen, S.Ch. Sarma, A. Bagger, M. Gong, S. Favero, C.-X. Zhao, R. Garcia-Serres, A.Y. Li, Q. Zhang, F. Jaouen, F. Maillard, A. Kucernak, I.E.L. Stephens, M.-M. Titirici, FeNC Oxygen Reduction Electrocatalyst with High Utilization Penta-Coordinated Sites, Adv. Mater. 35 (2023) 2211022. https://doi.org/10.1002/adma.202211022.
[62] S. Akula, H.-M. Piirsoo, A. Kikas, V. Kisand, M. Käärik, J. Leis, A. Treshchalov, J. Aruväli, K. Kukli, K. Tammeveski, ZIF-8-derived nanocarbon composite-based highly active platinum group metal-free bimetallic electrocatalysts for oxygen reduction reaction in proton exchange membrane fuel cells, Electrochim. Acta 498 (2024) 144691. https://doi.org/10.1016/j.electacta.2024.144691.
[63] H.A. Gasteiger, S.S. Kocha, B. Sompalli, F.T. Wagner, Activity benchmarks and requirements for Pt, Pt-alloy, and non-Pt oxygen reduction catalysts for PEMFCs, Appl. Catal. B 56 (2005) 9–35. https://doi.org/10.1016/j.apcatb.2004.06.021.
[64] A. Orfanidi, P.J. Rheinländer, N. Schulte, H.A. Gasteiger, Ink Solvent Dependence of the Ionomer Distribution in the Catalyst Layer of a PEMFC, J. Electrochem. Soc. 165 (2018) F1254. https://doi.org/10.1149/2.1251814jes.